Size of Cell-Surface Kv2.1 Domains is Governed by Growth Fluctuations

Aubrey V. Weigel,[†] Philip D. Fox,[‡] Elizabeth J. Akin,[‡] Kari H. Ecklund,[§] Michael M. Tamkun,[‡¶] and Diego Krapf[†§*]
[†]School of Biomedical Engineering, [‡]Department of Biomedical Sciences, [§]Department of Electrical and Computer Engineering, and [¶]Department of Biochemistry and Molecular Biology, Colorado State University, Fort Collins, Colorado

ABSTRACT   The Kv2.1 voltage-gated potassium channel forms stable clusters on the surface of different mammalian cells. Even though these cell-surface structures have been observed for almost a decade, little is known about the mechanism by which cells maintain them. We measure the distribution of domain sizes to study the kinetics of their growth. Using a Fokker-Planck formalism, we find no evidence for a feedback mechanism present to maintain specific domain radii. Instead, the size of Kv2.1 clusters is consistent with a model where domain size is established by fluctuations in the trafficking machinery. These results are further validated using likelihood and Akaike weights to select the best model for the kinetics of domain growth consistent with our experimental data.

INTRODUCTION

Membrane compartments or domains appear in many different cell types. These domains are varied in their composition and in the residence time that an individual molecule remains confined within the specific domain. The mechanisms by which a cell forms and maintains these specific structures in the plasma membrane can be very diverse, depending on the length and timescales involved. To name a few examples, MHC-I forms dynamic clusters with typical lifetimes of tens of seconds that are governed by the concerted action of exocytosis and the existence of cytoskeleton-based diffusion barriers (1,2). Both cadherin (3) and transferrin receptors (4) undergo transient confinement as they diffuse over the cell surface presumably due to transient trapping within various cytoskeletal domains. IgE receptors diffuse within micron-sized membrane domains defined by actin bundles, over timescales of seconds (5).

Hemagglutinin molecules form dynamic irregular clusters on length scales from 40 nm up to micrometers (6). In sharp contrast to these examples of membrane domains, the voltage-gated K^+ channel Kv2.1 forms micron-sized clusters that are stable over the course of hours. These surface domains appear in hippocampal neurons in vitro and in vivo (7–9), in spinal cord motor neurons (10), and in transfected HEK cells (11–15). Kv2.1 clusters are proposed to have a neuroprotective role in the mammalian brain (11). However, the physical mechanism behind cluster formation and maintenance is still unknown.

Within the brain, Kv2.1 regulates membrane excitability. Here it targets to cell surface domains on the soma, proximal dendrites, and axon initial segment (7). Unlike neurotransmitter receptors that statically tether to scaffolds, localization of Kv2.1 does not involve static tethering to cytoplasmic components. Instead, the channels are able to move within these domains displaying anomalous and confined subdiffusion, as seen by single-particle tracking (15,16). Even though it is observed that clustered Kv2.1 channels can escape from its confining domain to be eventually trapped into a different domain, these hopping phenomena occur very infrequently as compared to trafficking via insertion and retrieval pathways (17). Along these lines, we have recently shown that Kv2.1 channels directly traffic from the cytosol to Kv2.1 clusters and vice versa (17).

Insertion of channels into the plasma membrane occurs solely at the perimeter of clusters via a vesicle docking and delivery mechanism. Similarly, internalization of Kv2.1 channels occurs from the cluster perimeter. However, the question of how the cell regulates Kv2.1 domain size remains unanswered. Given that delivery and internalization of potassium channels takes place at the cluster perimeter (17), the cellular trafficking machinery has some seeming knowledge of the cluster location. Therefore, it is tempting to hypothesize that cluster sizes are actively regulated by balancing internalization and exocytosis events via a feedback mechanism. Alternatively, cluster sizes may be left to the fate of fluctuations in the exocytic/endocytic machinery. Even though this latter pathway lacks some degree of control it has the advantage of being favorable from an energy budget perspective.

Here, we study the Kv2.1 domain size distribution on the surface of HEK cells to shed light into the mechanism by which Kv2.1 clusters are regulated. We use a simple growth model to investigate the distribution of domain sizes in a similar fashion to Gov's model (18) for the size distribution of focal adhesions. The size distribution is directly linked to the maintenance and regulation of domains. For example, if a feedback mechanism maintained a specific domain size by locally balancing endocytosis and exocytosis, this preferred size would have the highest probability. Thus, the probability density of domain radii would peak at this specific value. In general, the evolution of cluster size distribution

can be modeled, in the continuum approximation, by a Fokker-Planck equation, which makes a direct connection between the kinetic model of growth and the size distribution (19). The Fokker-Planck equation in one variable is derived from the stochastic differential equation

$$\frac{dx}{dt} = v_c(x) + v_f(t),$$

where v_c is a deterministic velocity and v_f is a stochastic quantity. We have ignored any inertial terms that are not relevant to growth models. The fluctuations in the velocity are often assumed to be δ-correlated,

$$\langle v_f(t)v_f(t')\rangle = 2D\delta(t - t'), \tag{1}$$

and the corresponding Fokker-Planck equation for the distribution function $P(x,t)$ is (20)

$$\frac{dP}{dt} = -\frac{\partial}{\partial x}[v_c(x)P] + D\frac{\partial^2 P}{\partial x^2}. \tag{2}$$

Using this formalism, we find that the size distribution of Kv2.1 domains is governed by fluctuations in the trafficking pathways and that no local feedback exists between endocytosis and exocytosis.

MATERIALS AND METHODS

Cell culture and transfection

Kv2.1 channels labeled with an intracellular GFP at the N-terminus have been used previously (GFP-Kv2.1 (13–15)). Human embryonic kidney (HEK) 293 cells (passage 38–45; American Type Culture Collection, Manassas, VA) were kept in Dulbecco's Modified Eagle's Medium (DMEM; Gibco, Life Technologies, Carlsbad, CA) supplemented with 10% fetal bovine serum (FBS; Gibco) at 37°C and 5% CO_2. Cells were transfected by electroporation using a Genepulser Xcell (BioRad Laboratories, Hercules, CA) with a 0.2-cm gap cuvette and a single 110-V 25-ms pulse with 3 μg of GFP-Kv2.1 expressing DNA. After electroporation, cells were plated on cover-glass-bottom culture dishes that had been previously Matrigel-coated (BD Biosciences, San Jose, CA) and covered in DMEM without Phenol Red (Life Technologies) and 10% FBS. Cells were used for live cell imaging within 24 h of transfection.

Live cell imaging

Before imaging, cells were always rinsed twice with a HEK physiological imaging saline consisting of 146 mM NaCl, 4.7 mM KCl, 2.5 mM $CaCl_2$, 0.6 mM $MgSO_4$, 1.6 mM $NaHCO_3$, 0.15 mM NaH_2PO_4, 0.1 mM ascorbic acid, 8 mM glucose, and 20 mM HEPES, pH 7.4. Cells expressing fluorescent protein-tagged constructs were imaged in an imaging saline at 37°C in a homebuilt, objective-type total internal fluorescence (TIRF) microscope built around a model No. IX71 (Olympus, Melville, NY) (15). Green fluorescent protein (GFP) was excited using a 473-nm diode pumped solid-state laser (Shanghai Dream Lasers, Shanghai, China). The beam was expanded, recollimated, attenuated with a neutral density filter to yield 2.5 mW after the objective, and focused at the back focal plane of a 100× objective (PlanApo N.A. 1.45; Olympus) using an antireflection-coated achromatic doublet with a focal length of 400 mm (Thorlabs, Newton,

NJ). The GFP fluorescence was collected in an electron-multiplied charge-coupled device (iXon DU-888; Andor Technology, Belfast, Ireland). Both the dish and the objective were maintained at 37°C using a temperature control system (Bioptechs, Butler, PA).

Image and data analysis

Images were acquired using IQ 2.3 software (Andor Technology) and saved as 16-bit tiff files. The images were analyzed with a custom-written algorithm in LabVIEW (National Instruments, Austin, TX). We manually selected the center of each cluster, and then the intensity of the pixels in the horizontal and vertical cross sections of the clusters was generated. These line profiles were fit to Gaussian functions using the Levenberg-Marquardt least-square method. The LabVIEW codes used to perform this analysis are available upon request. The obtained data were imported into the software Origin 8.1 (OriginLabs, Northampton, MA) for further processing.

Cytoskeleton disruption reagents

Latrunculin A (LatA; Sigma-Aldrich, St. Louis, MO) was used to disrupt the cortical actin. In these experiments, LatA was dissolved in dimethyl sulfoxide (DMSO; Sigma-Aldrich) and directly added to the imaging dish to a final concentration of 100 nM (16). Cells were imaged up to 20 min after drug application. DMSO-only controls showed no evident effect on Kv2.1 clusters.

Models

In general, the three different types of domain growth without any feedback mechanism are:

1. channels that exchange with a reservoir, i.e., the membrane outside the domains, by permeating through the domain perimeter;
2. channels that are directly inserted from the cytosol into the interior of the domain and are retrieved from the interior of the domain to the cytosol; and
3. a constant inward/outward flux that is directly maintained independent of domain size.

The first two models of growth were given by Gov (18) and are also reproduced here for convenience. A fourth model is also given below for a feedback mechanism between growth rate and cluster size.

Model 1

The mass balance equation for a domain with area A, allowed to grow only by permeation through its perimeter is

$$\frac{\partial A}{\partial t} = -k_{off}r + k_{on}nr, \tag{3}$$

where k_{on} and k_{off} are the on- and off-rates, n is the surrounding mean protein density, and r is the radius of the domain, such that $A = \pi r^2$. Replacing variables in Eq. 3, we get the equation of motion for the radius r,

$$\frac{\partial r}{\partial t} = \frac{-k_{off}}{2\pi} + \frac{k_{on}n}{2\pi}. \tag{4}$$

From Eqs. 2 and 4, we can write the corresponding Fokker-Planck equation for the radius probability density function (PDF),

$$\frac{\partial P}{\partial t} = -\frac{1}{2\pi}\left(k_{on}n - k_{off}\right)\frac{\partial P}{\partial r} + D\frac{\partial^2 P}{\partial r^2}. \tag{5}$$

The noise term D accounts for temporal fluctuations in the insertion and retrieval of molecules into and out of a cluster (given by Eq. 1) and results in an effective broadening of the distribution. Sources of fluctuations include ATP and GTP availability (for the action of motors and GTPases), obstruction by intracellular compartments, anomalous Brownian motion of channels to arrive to endocytic pits, dynamic distribution of microtubules, etc. Fluctuations in the trafficking machinery are assumed to be intrinsic to the endocytic and exocytic machinery and to have δ-function correlations (21,22). The resulting steady-state solution to Eq. 5 is an exponential in r,

$$P_1(r) = R_n e^{-r\left(k_{off} - k_{on}n\right)/2\pi D}, \tag{6}$$

where R_n is a normalization constant.

Model 2

When we consider a domain that can grow at any point in its interior,

$$\frac{\partial A}{\partial t} = -k_{off}A + k_{on}nA, \tag{7}$$

the corresponding Fokker-Planck equation is

$$\frac{\partial P}{\partial t} = -\left(k_{on}n - k_{off}\right)\frac{\partial(AP)}{\partial A} + D\frac{\partial^2 P}{\partial A^2}. \tag{8}$$

The resulting PDF is a Gaussian in A,

$$P_2(A) = R_n e^{-A^2\left(k_{off} - k_{on}n\right)/2D}, \tag{9}$$

or, by changing variables,

$$P_2(r) = R_n r e^{-\pi^2 r^4\left(k_{off} - k_{on}n\right)/2D}. \tag{10}$$

Model 3

In the last case, when there is a constant source and sink, we have the mass balance equation

$$\frac{\partial A}{\partial t} = -k_{off} + k_{on}n, \tag{11}$$

with the corresponding Fokker-Planck equation

$$\frac{\partial P}{\partial t} = -\left(k_{on}n - k_{off}\right)\frac{\partial P}{\partial A} + D\frac{\partial^2 P}{\partial A^2}. \tag{12}$$

The resulting PDF is an exponential in A,

$$P_3(A) = R_n e^{-A\left(k_{off} - k_{on}n\right)/D} \tag{13}$$

and

$$P_3(r) = R_n r e^{-\pi r^2\left(k_{off} - k_{on}n\right)/D}. \tag{14}$$

Model 4

A different model of growth takes place when feedback exists between on- and off-rates, to maintain a given domain size. The coupling of growth rates to the size of the domain can be modeled in different ways. A simple approach to this problem is to have an insertion term that is dependent on cluster size so that $k_{on}n = k_{off}$ when $r = R_0$, $k_{on}n$ decreases when $r > R_0$, and

$k_{on}n$ increases when $r < R_0$. In a proportional negative feedback control (linear approximation),

$$k_{on}n = k_{off} + \alpha(R_0 - r), \tag{15}$$

where α is a coupling constant with units of s^{-1}, i.e., the proportional gain. Then, assuming the domain grows by permeation through its perimeter,

$$\frac{\partial A}{\partial t} = -k_{off}r + k_{on}nr = \alpha(R_0 - r)r, \tag{16}$$

$$\frac{\partial r}{\partial t} = \frac{\alpha}{2\pi}(R_0 - r), \tag{17}$$

$$\frac{\partial P}{\partial t} = -\frac{\alpha}{2\pi}\frac{\partial}{\partial r}\left[(R_0 - r)P\right] + D\frac{\partial^2 P}{\partial r^2}. \tag{18}$$

This Fokker-Planck equation has the steady-state solution

$$P_4(r) = R_n e^{\alpha\left(2R_0 r - r^2\right)/4\pi D}, \tag{19}$$

which grows exponentially for values $r \ll R_0$, is a Gaussian tail for large radii, and peaks at $r = R_0$. In Models 1–3, the off-rate must be larger than the on-rate for the distributions to be normalizable (18). This constraint is naturally taken care of within the feedback model. Other types of feedback mechanisms can be formulated but little is gained by studying them in the context of Kv2.1 domain radii. As an example, a different formalism is presented in the Appendix.

RESULTS AND DISCUSSION

Characterization of the distribution of domain radii

Fig. 1 A shows a TIRF image of the basal surface of a cell expressing Kv2.1 channels tagged with GFP. Kv2.1 domains are visible as spots with high intensity levels. The size of the apparent domains is measured by fitting the intensity cross-section profile of each spot to a Gaussian curve (as shown, for a typical domain, in Fig. 1 B). The full width at half-maximum of the Gaussian curve provides a good estimate of the diameter of the domain. In our analysis, we have included clusters that are either circular or elliptical. Irregularly-shaped domains, accounting for only 5% of the total clusters, are discarded to avoid including two domains into a single fit. The probability distribution of cluster radii built from the measurement of 674 radii in 16 different cells is shown in Fig. 2. For each cluster, two radii are obtained: the first one from the vertical cross section and the second one from the horizontal cross section, as indicated in Fig. 1 B. Both radii are included in the distribution. As is apparent in Fig. 2, the obtained distribution is an exponential decay.

Two correlated effects limit the sensitivity of our size measurements. On the one hand, when a domain is too small, the intensity profile width is dictated by the point spread function (PSF) independent of domain size. In general, the image is given by the convolution of the PSF
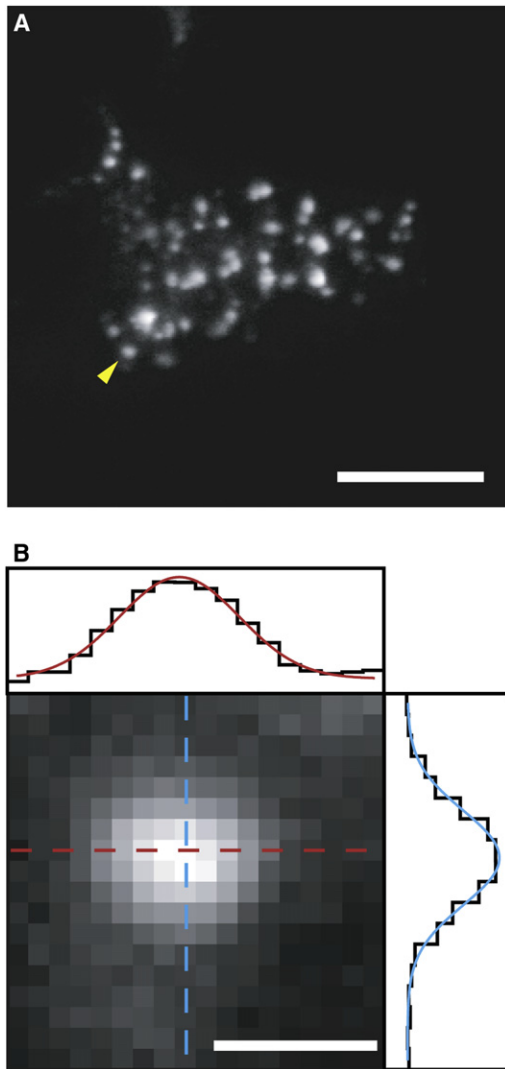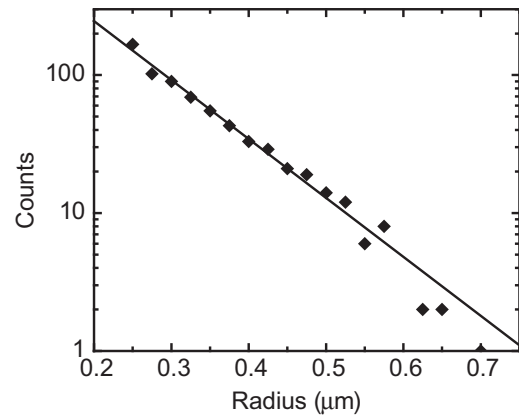
FIGURE 2 Distribution of cluster radii obtained from fitting Gaussian functions to the intensity profile of the cross-sections of each cluster. The line shows a fit to $R_n\exp(-\lambda r)$.

FIGURE 1 GFP-Kv2.1 clusters in the basal membrane of transfected HEK293 cells. (*A*) TIRF image showing clusters in a cell. Scale bar is 10 μm. (*B*) Zoom of the cluster (*yellow arrow*). The two cross-section intensity profiles are fit to a Gaussian curve. Scale bar is 1 μm. Pixel size is 0.13 μm.

Fig. 3). Then, a domain with five channels has a diameter of 0.5 μm. Therefore, these structures do not suffer from limitations in the resolution imposed by the system's PSF described above.

The probability density function of domain radii fits well to an exponential distribution. This is consistent with a mode of growth where channels are inserted into and extracted from the clusters by exchange with a channel reservoir crossing the domain boundaries, i.e., Model 1 as described in Materials and Methods. At first sight, this hypothesis appears to contradict measurements showing that the main pathway of channel trafficking to and from the Kv2.1 clusters is via endocytic and exocytic mechanisms (17). In Deutsch et al. (17), we used quantum-dot labeling and TIRF imaging approaches to show that Kv2.1 clusters are specialized platforms involved in the trafficking of membrane proteins to and from the cell surface. This approach enabled us to track individual channels and to directly detect the location of plasma membrane insertion

and the observed structure. In our setup, the PSF can be roughly approximated by a two-dimensional Gaussian with a full width at half-maximum of 350 nm. Thus, the smallest spots will appear to have an effective diameter of 350 nm. On the other hand, when the number of channels is small, the definition of a cluster as a circular domain with a well-defined perimeter is not applicable. Namely, the perimeter of the area occupied by structures containing two or three channels is poorly defined. To deal with this problem, we obtained the number of channels in each spot and consider only domains that contain at least five channels. Channel number quantification was performed by measuring discrete photobleaching steps of individual GFP tags as described in the Supporting Material. We found that the density of channels in the clusters was 27.8 $\pm$ 8.7 channels per μm^2 (mean $\pm$ standard deviation, $n = 53$,
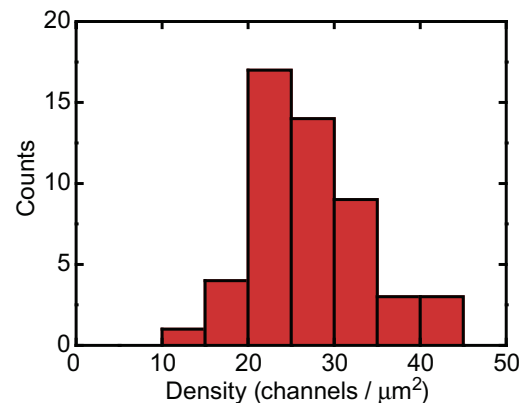

FIGURE 3 Density of Kv2.1 channels inside clusters. The number of channels is recorded as described in the text and the area is computed as $\pi d_1 d_2/4$, where d_1 and d_2 are the diameters found from the cross sections of the cluster intensity profiles.

of Kv2.1 channels as well as the location of endocytosis from the surface. We observed that Kv2.1 clusters represent platforms for the insertion and retrieval of not only Kv2.1 but also the unrelated K^+ channel, Kv1.4.

A different explanation to the apparent growth mode, which is consistent with our previous observations, is that the number of endocytic/exocytic spots is proportional to the domain perimeter. The measured domain size distribution implies that the rate of channel trafficking to and from the cluster is proportional to the domain circumference length. Thus, these results are in agreement with the hypothesis that the larger the cluster, the higher the probability of introducing a trafficking spot and, therefore, the number of these spots grows linearly with domain radius.

The type of growth described by Eq. 3 assumes no explicit correlation between cluster size and on-/off-rates. If the growth rates were controlled by a feedback mechanism that actively maintained a constant domain size, the probability density function of radii would peak at some given value. This can be achieved via an on-rate that increases above the off-rate when the domain shrinks, as modeled by Eq. 15. However, the distribution of radii monotonically decreases (see Fig. 2), which suggests that no feedback exists between the growth rates and the domain size. The selection of the exponential distribution over the other potential models is rigorously confirmed in the next section through the Akaike information criterion.

Model 1 implies that removal is more predominant than delivery, $k_{off} > k_{on}n$. Otherwise, the domains would grow indefinitely. In the limiting case that fluctuations in the endocytic/exocytic machinery were negligible, the steady-state solution to this model would be nonzero only for $r = 0$. In other words, because endocytosis dominates over exocytosis, all domains would disappear. However, temporal fluctuations in the on-/off-rates lead to a finite broadening of the distribution of domain sizes. The strength of these fluctuations is characterized by the parameter D. From the distribution of radii we find the relative magnitude of the fluctuations in the on-/off-rate is $D/k_{off} - k_{on}n) = 15$ nm.

Model selection

The semi-log histogram depicted in Fig. 2 is indicative of a population of Kv2.1 surface domains that are merely controlled by fluctuations in the endocytosis and exocytosis machinery. However, it is desirable to quantify the likeliness of the proposed model by considering alternative distributions and performing goodness-of-fit tests. The simple and widely used approach of fitting histograms to a model distribution can be problematic due to binning artifacts and the lack of consideration of bins with zero counts. To avoid these drawbacks, alternative competing hypotheses can be considered. Then, biological inferences can be drawn by model selection grounded in likelihood theory (23). Model

selection is generally used to select the model that is best supported by the experimental data.

We performed a test based on the statistical theory of likelihood that circumvents the problems described above. Techniques of model selection use negative log-likelihood as a metric for lack-of-fit. Several criteria for model selection exist. The Akaike information criterion (AIC) is the approach of choice in most cases (23,24). AIC estimates the Kullback-Leibler information lost by approximating the experimental data to the fitting model (25). A drawback of AIC is that it is biased toward models that are more complex. On the other hand, the Bayesian information criterion favors the simpler model. Nevertheless, we see that in the analysis of domain size distribution the model selection using AIC yields the simplest model and, thus, complexity bias is not a concern.

Our approach is based on the Akaike information criterion to determine whether our measured set of domain radii provides evidence for one of the proposed hypotheses. AIC quantifies the relative support for each competing model. Given the measured radii $\textbf{\textit{r}}$, we can obtain the log-likelihood function for model i ($i = 1, 2, 3, 4$),

$$\ln[L_i(\lambda|\text{data } \textbf{\textit{r}})],$$

where λ is the set of unknown parameters. Details of the methods used to obtain the log-likelihood functions and the sets of parameters λ of each model are given in the Appendix. The AIC for each model is given by

$$\text{AIC}_i = -2\ln\left[L_i\left(\widehat{\lambda}_i|\text{data } \textbf{\textit{r}}\right)\right] + 2p_i, \qquad (20)$$

where p_i is the number of free parameters and $\widehat{\lambda}_i$ is the maximum likelihood estimate of parameters λ_i, for model i. Then, the AIC differences are $\Delta_i = \text{AIC}_i - \text{AIC}_{\text{min}}$. The relative weight of evidence for each model is known as the Akaike weight and is given by

$$w_i = \frac{\exp(-\Delta_i/2)}{\sum_j \exp\left(-\Delta_j/2\right)}. \qquad (21)$$

The Akaike weights are values between 0 and 1 that can be interpreted as the probability that a given model is the best approximating model for the measured data. Table 1 shows the weights of each of the models described in Materials and Methods. In good agreement with the semi-log plot of the histogram (Fig. 2), the model by which the on- and off-rates are linearly proportional to the perimeter of the domain, i.e., Model 1, is strongly supported by the data. This model has a relative likelihood of 94% as compared to the other hypotheses.

The model that describes growth rates involving the insertion of molecules directly into the domains, not involving the perimeter, has the lowest likelihood. The ratio of its

TABLE 1 Analysis of the Kv2.1 sizes from control cells

Model	Maximum likelihood estimates	Δ_i	w_i
1: Perimeter-dependent growth	$\lambda_1 = 10.7 \ \mu m^{-1}$	0	0.94
2: Bulk-dependent growth	$\lambda_2 = 45.3 \ \mu m^{-4}$	98.9	10^{-20}
3: Size-independent growth	$\lambda_3 = 16.6 \ \mu m^{-2}$	5.4	0.06
4: Feedback regulation	$\lambda_4 = 35.6 \ \mu m^{-2}$, $R_0 = 0.25 \ \mu m$	22.5	10^{-5}
	$\lambda_4 = 44.6 \ \mu m^{-2}$, $R_0 = 0.30 \ \mu m$	56.2	10^{-13}

AIC applied to the four distributions described in Materials and Methods over the interval $r \geq 0.25 \ \mu m$. The Δ_i values are the AIC differences and w_i the Akaike weights. The maximum likelihood estimates are $\lambda_1 = \pi(k_{off} - k_{on}n)/2\pi D$, $\lambda_2 = \pi^2(k_{off} - k_{on}n)/2D$, $\lambda_3 = \pi(k_{off} - k_{on}n)/D$, and $\lambda_4 = \alpha/4\pi D$. Note that the definitions and the units of k_{on} and k_{off} are model-dependent according to Eqs. 1, 5, 9, and 13. For Model 4, two different values of R_0 are reported to indicate the fast decay of the likelihood with R_0.

likelihood to the likelihood of the perimeter-dependent hypothesis is 10^{-20}. This is in agreement with our experimental observations that insertion and retrieval of Kv2.1 channels occurs primarily at the cluster perimeter, emphasizing the accuracy of the used statistical criteria.

The feedback mechanism described by Model 4 was tested for values of $R_0 \geq 0.25 \ \mu m$. This is the minimum value of well-defined clusters and, thus, the proposed feedback mechanism aimed at stabilizing clusters to R_0 is not relevant for smaller values of R_0. The highest likelihood of this model was obtained for $R_0 = 0.25 \ \mu m$, but it was several orders-of-magnitude smaller than the models not involving any feedback control. The likelihood decreased very fast for larger values of R_0, indicating the lack of evidence for this model. Even though the number of models discussed here is not necessarily exhaustive, the goodness-of-fit of the exponential distribution is remarkable.

Changes in the kinetics of growth affect domain size distribution

As a control experiment of our distribution analysis, we sought to introduce changes in the growth kinetics of Kv2.1 microdomains. One way to drastically alter Kv2.1 clusters is to disrupt the cortical actin cytoskeleton (15,16). The effect of cortical actin disruption on Kv2.1 is complex, as treatment with different pharmacological inhibitors of actin can cause clusters to dissolve or fuse depending on the concentration applied. We used the G-actin sequestering agent LatA (26) to inhibit the polymerization of actin and induce coalescence of Kv2.1 clusters. Upon treatment with 100 nM LatA, Kv2.1 clusters become more dynamic and merge (see Movie S1 and Movie S2 in the Supporting Material). We then examined whether there is a measurable change in the cluster size distribution induced by the disruption of cortical actin. If the distribution of radii were sensitive to the physical mechanism of cluster maintenance, pharmacological treatment with an actin polymerization inhibitor should induce an observable change in this distribution.

The radii of Kv2.1 domains in seven different cells were measured immediately before and 10 min after LatA application. We observed that, after treatment, not only did the total number of clusters decrease from 767 to 248, but their average size also increased, as expected from the aggregation of clusters (see Movie S2). This is can be seen in the images of a cell before (Fig. 4 A) and 10 min after (Fig. 4 B) LatA application. Additionally Fig. 4 C shows the mean area of the clusters. After a lag phase of 300 s, a dramatic fivefold increase in size is seen as LatA takes effect. A complementary analysis of the effect of actin on domain dynamics is presented in the Supporting Material. As shown in Fig. 4 D, the distribution of radii 10 min after Lat A addition is no longer an exponential for the probed
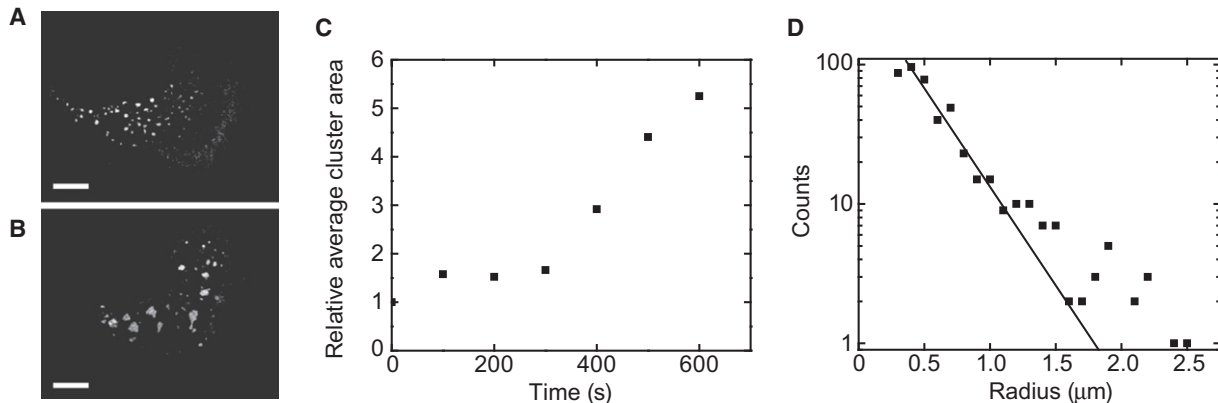

FIGURE 4 Cells treated with LatA. (A) TIRF image showing Kv2.1 clusters immediately before LatA application. The scale bar is 10 μm. (B) Same cell, 10 min after addition of LatA. The number of Kv2.1 clusters has decreased and their area clearly increased. (C) Time-course of the average cluster size in a single cell after application of LatA. The cluster area was normalized to the average area of the clusters immediately before LatA application. The addition of LatA occurs at time zero. LatA appears to take effect 300 s after application. Until this time, the cluster size distribution remains in steady state. (D) Distribution of cluster radii in cells treated with the actin inhibitor LatA. (Straight line) Distribution $R_n \exp(-\lambda r)$.

range. Instead, a slower decay is observed with larger domains being prominent.

Our simple measurement of the distribution of domain sizes shows that the growth model is affected by inhibition of cortical actin and, in turn, the distribution of cluster sizes changes. Unfortunately, the information theory analysis used in control cells cannot be applied to the LatA-treated cells because, as seen in Fig. 4 C, in this case the domain size distribution is not in steady state. Nevertheless, a change is directly seen in the dynamic cluster size distribution, which provides further evidence for the link between the distribution of domain sizes and the membrane compartmentalization mechanism.

CONCLUSIONS

The distribution of domain sizes provides a straightforward method for obtaining kinetic information on the formation and maintenance of membrane domains. The strength of this method lies in its simple application. The distribution of Kv2.1 domain sizes implies that cluster growth is proportional to the cluster perimeter length. Additionally, we do not find evidence for local feedback between endocytic and exocytic events at the individual cluster level. The model scenarios analyzed in this work are not exhaustive, and other kinetic models can be proposed, in particular at longer length scales. The likelihood of the proposed model was rigorously established through the Akaike information criterion. The distribution analysis is consistent with a model where the cluster size is simply governed by the fluctuations of the endocytic and exocytic processes.

APPENDIX: LOG-LIKELIHOOD FUNCTIONS

Function 1 (Model 1)

The normalization constant in Eq. 6 is found from

$$\int_a^\infty P_1(r)dr = 1,$$

where a is the minimum radius that can be assigned to a domain. Then,

$$R_n = \lambda \exp(\lambda a), \quad (A1)$$

where

$$\lambda = \frac{(k_{off} - k_{on}n)}{2\pi D}.$$

Then, the log-likelihood function is

$$\ln[L_1(\lambda|\boldsymbol{r})] = n \ln n + n\lambda a - \lambda \sum_i^n r_i, \quad (A2)$$

where $r = \{r_1, r_2, ..., r_n\}$ is our data set and L_1 is the likelihood of the parameter λ, given the data set.

Function 2 (Model 2)

The normalization constant in Eq. 10 is

$$R_n = 4\sqrt{\frac{\lambda}{\pi}}\left[\text{erfc}\left(a^2\sqrt{\lambda}\right)\right]^{-1}, \quad (A3)$$

where

$$\lambda = \pi^2\frac{(k_{off} - k_{on}n)}{2D},$$

and *erfc* is the complementary error function defined as

$$\text{erfc}(x) = \left(\frac{2}{\sqrt{\pi}}\right)\int_x^\infty \exp(-t^2)dt.$$

The log-likelihood function is

$$\begin{aligned}\ln[L_2(\lambda|\boldsymbol{r})] = {} & \frac{n}{2} \ln\left(\frac{16\lambda}{\pi}\right) - n \ln\left[\text{erfc}\left(a^2\sqrt{\lambda}\right)\right] \\ & + \sum_j^n \ln r_j - \lambda \sum_i^n r_i^4.\end{aligned} \quad (A4)$$

Function 3 (Model 3)

The normalization constant in Eq. 14 is

$$R_n = 2\lambda \exp(a^2\lambda), \quad (A5)$$

where

$$\lambda = \pi\frac{(k_{off} - k_{on}n)}{D}.$$

The log-likelihood function is

$$\ln[L_3(\lambda|\boldsymbol{r})] = n \ln(2\lambda) + na^2\lambda + \sum_j^n \ln r_j - \lambda \sum_i^n r_i^4. \quad (A6)$$

Function 4 (Model 4)

The normalization constant in Eq. 19 is

$$R_n = \frac{2\sqrt{\lambda/\pi}\exp(-\lambda R_0^2)}{\text{erfc}\left[(a - R_0)\sqrt{\lambda}\right]}, \quad (A7)$$

where $\lambda = \alpha/4\pi D$.

The log-likelihood function is

$$\begin{aligned}\ln[L_4(\lambda, R_0|\boldsymbol{r})] = {} & \frac{n}{2} \ln\left(\frac{4\lambda}{\pi}\right) + nR_0^2\lambda \\ & - n \ln\left[\text{erfc}\left[(a - R_0)\sqrt{\lambda}\right]\right] \\ & + 2\lambda R_0 \sum_j^n r_j - \lambda \sum_i^n r_i^2.\end{aligned} \quad (A8)$$

Function 5 (alternative to Model 4)

We also considered a different feedback mechanism as an alternative to Model 4. In Model 4, we maintain a radius-dependent on-rate with molecules being incorporated at the domain perimeter. However, in a similar fashion to Model 3, we consider a model where the growth is radius-dependent but the incorporation of new molecules is independent of domain size. Thus,

$$\frac{\partial A}{\partial t} = \alpha(R_0 - r). \tag{A9}$$

The corresponding Fokker-Planck equation is

$$\frac{\partial P}{\partial t} = -\frac{\alpha}{\sqrt{\pi}}\frac{\partial}{\partial A}\left[\left(\sqrt{\pi}R_0 - \sqrt{A}\right)P\right] + D\frac{\partial^2 P}{\partial A^2}. \tag{A10}$$

In steady state, we obtain

$$P_5(A) = R_n e^{Z_1 A - Z_2 A^{3/2}}, \tag{A11}$$

where

$$Z_1 = \frac{\alpha R_0}{D} \text{ and } Z_2 = \frac{2\alpha}{(3\sqrt{\pi}D)}.$$

Then,

$$P(r) = R_n r e^{\alpha\pi\left(3R_0 r^2 - 2r^3\right)/3D}. \tag{A12}$$

The likelihood of this model is found to be smaller than that of Model 4.

SUPPORTING MATERIAL

Two figures, supporting text, and two movies are available at http://www.biophysj.org/biophysj/supplemental/S0006-3495(12)01026-0.

REFERENCES

1. Lavi, Y., M. A. Edidin, and L. A. Gheber. 2007. Dynamic patches of membrane proteins. *Biophys. J.* 93:L35–L37.

2. Lavi, Y., N. Gov, …, L. A. Gheber. 2012. Lifetime of major histocompatibility complex class-I membrane clusters is controlled by the actin cytoskeleton. *Biophys. J.* 102:1543–1550.

3. Kusumi, A., K. Suzuki, and K. Koyasako. 1999. Mobility and cytoskeletal interactions of cell adhesion receptors. *Curr. Opin. Cell Biol.* 11:582–590.

4. Sako, Y., and A. Kusumi. 1995. Barriers for lateral diffusion of transferrin receptor in the plasma membrane as characterized by receptor dragging by laser tweezers: fence versus tether. *J. Cell Biol.* 129:1559–1574.

5. Andrews, N. L., K. A. Lidke, …, D. S. Lidke. 2008. Actin restricts FcεRI diffusion and facilitates antigen-induced receptor immobilization. *Nat. Cell Biol.* 10:955–963.

6. Hess, S. T., T. J. Gould, …, J. Zimmerberg. 2007. Dynamic clustered distribution of hemagglutinin resolved at 40 nm in living cell membranes discriminates between raft theories. *Proc. Natl. Acad. Sci. USA.* 104:17370–17375.

7. Sarmiere, P. D., C. M. Weigle, and M. M. Tamkun. 2008. The Kv2.1 K$^+$ channel targets to the axon initial segment of hippocampal and cortical neurons in culture and in situ. *BMC Neurosci.* 9:112.

8. Kihira, Y., T. O. Hermanstyne, and H. Misonou. 2010. Formation of heteromeric Kv2 channels in mammalian brain neurons. *J. Biol. Chem.* 285:15048–15055.

9. Guan, D. X., L. R. Horton, …, R. C. Foehring. 2011. Postnatal development of A-type and Kv1- and Kv2-mediated potassium channel currents in neocortical pyramidal neurons. *J. Neurophysiol.* 105:2976–2988.

10. Muennich, E. A., and R. E. Fyffe. 2004. Focal aggregation of voltage-gated, Kv2.1 subunit-containing, potassium channels at synaptic sites in rat spinal motoneurones. *J. Physiol.* 554:673–685.

11. Misonou, H., D. P. Mohapatra, …, J. S. Trimmer. 2005. Calcium- and metabolic state-dependent modulation of the voltage-dependent Kv2.1 channel regulates neuronal excitability in response to ischemia. *J. Neurosci.* 25:11184–11193.

12. Mohapatra, D. P., and J. S. Trimmer. 2006. The Kv2.1 C terminus can autonomously transfer Kv2.1-like phosphorylation-dependent localization, voltage-dependent gating, and muscarinic modulation to diverse Kv channels. *J. Neurosci.* 26:685–695.

13. O'Connell, K. M., and M. M. Tamkun. 2005. Targeting of voltage-gated potassium channel isoforms to distinct cell surface microdomains. *J. Cell Sci.* 118:2155–2166.

14. Tamkun, M. M., K. M. O'Connell, and A. S. Rolig. 2007. A cytoskeletal-based perimeter fence selectively corrals a sub-population of cell surface Kv2.1 channels. *J. Cell Sci.* 120:2413–2423.

15. Weigel, A. V., B. Simon, …, D. Krapf. 2011. Ergodic and nonergodic processes coexist in the plasma membrane as observed by single-molecule tracking. *Proc. Natl. Acad. Sci. USA.* 108:6438–6443.

16. O'Connell, K. M., A. S. Rolig, …, M. M. Tamkun. 2006. Kv2.1 potassium channels are retained within dynamic cell surface microdomains that are defined by a perimeter fence. *J. Neurosci.* 26:9609–9618.

17. Deutsch, E., A. V. Weigel, …, M. M. Tamkun. 2012. Kv2.1 cell surface clusters are insertion platforms for ion channel delivery to the plasma membrane. *Mol. Biol. Cell.* 23:2917–2929.

18. Gov, N. S. 2006. Modeling the size distribution of focal adhesions. *Biophys. J.* 91:2844–2847.

19. Jesson, D. E., T. P. Munt, …, D. Bimberg. 2004. Tunable metastability of surface nanostructure arrays. *Phys. Rev. Lett.* 92:115503.

20. Risken, H. 1989. The Fokker-Planck Equation: Methods of Solutions and Applications. Springer, Berlin, Germany.

21. Sornette, D., and R. Cont. 1997. Convergent multiplicative processes repelled from zero: power laws and truncated power laws. *J. Phys. I Fr.* 7:431–444.

22. Gov, N. S. 2009. Physical model for the width distribution of axons. *Eur. Phys. J E Soft Matter.* 29:337–344.

23. Johnson, J. B., and K. S. Omland. 2004. Model selection in ecology and evolution. *Trends Ecol. Evol. (Amst.).* 19:101–108.

24. Edwards, A. M., R. A. Phillips, …, G. M. Viswanathan. 2007. Revisiting Lévy flight search patterns of wandering albatrosses, bumblebees and deer. *Nature.* 449:1044–1048.

25. Burnham, K. P., and D. Anderson. 2002. Model Selection and Multi-Model Inference: A Practical Information-Theoretic Approach. Springer, New York, NY. 49–148.

26. Coué, M., S. L. Brenner, …, E. D. Korn. 1987. Inhibition of actin polymerization by latrunculin A. *FEBS Lett.* 213:316–318.